

Enhanced Surf Zone and Wave Runup Observations with Hovering Drone-Mounted Lidar^o

JULIA W. FIEDLER,^a LAUREN KIM,^a ROBERT L. GRENZEBACK,^a ADAM P. YOUNG,^a AND MARK A. MERRIFIELD^a

^a*Scripps Institution of Oceanography, La Jolla, California*

(Manuscript received 15 March 2021, in final form 30 August 2021)

ABSTRACT: We demonstrate that a hovering, drone-mounted laser scanner (lidar) paired with a survey-grade satellite and inertial positioning system measures the wave transformation across the surf zone and the resulting runup with accuracy almost equal to a stationary truck-mounted terrestrial lidar. The drone, a multirotor small uncrewed aircraft system (sUAS), provides unobstructed measurements by hovering above the surf zone at 20-m elevation while scanning surfaces along a 150-m-wide cross-shore transect. The drone enables rapid data collection in remote locations where terrestrial scanning may not be possible. Allowing for battery changes, about 17 min of scanning data can be acquired every 25 min for several hours. Observations were collected with a wide ($H_s = 2.2$ m) and narrow ($H_s = 0.8$ m) surf zone, and are validated with traditional land-based survey techniques and an array of buried pressure sensors. Thorough postprocessing yields a stable ($\bar{\sigma} = 1.7$ cm) back beach topography estimate comparable to the terrestrial lidar ($\bar{\sigma} = 0.8$ cm). Statistical wave properties and runup values are calculated, as well as bathymetry inversions using a relatively simple nonlinear correction to wave crest phase speed in the surf zone, illustrating the utility of drone-based lidar observations for nearshore processes.

SIGNIFICANCE STATEMENT: Small uncrewed aircraft systems (sUAS) equipped with lidar provide mobile and rapid data collection in remote locations or in response to extreme events. Precise positioning with survey-grade navigation tools gives the drone the capability to hover in place and obtain data similar in quality to a ground-based lidar system for limited time periods. Here, we present the use of hovering drone-mounted lidar to measure and calculate surf zone wave properties, wave up and down rushes at the shoreline, and water depth along a cross-shore transect extending over 100 m from the shoreline. Future use of hovering lidar-equipped sUAS will enable accurate nearshore observations at previously inaccessible sites and provide high-quality validation for surf zone and coastal flooding models.

KEYWORDS: Coastlines; Wave properties; Instrumentation/sensors; Lidars/Lidar observations; Remote sensing

1. Introduction

Coastal flooding is projected to increase in frequency and magnitude over the next century, resulting from processes that occur on time scales of seconds to millennia (e.g., Thompson et al. 2019; Tebaldi et al. 2012; Sweet and Park 2014; and others). On time scales of seconds to minutes, wave-driven runup—the alternating up and down rushes of water on the beach face—plays a significant role in determining the severity of coastal erosion and flooding (Serafin et al. 2017; Vitousek et al. 2017). Measuring, understanding, and modeling the forces leading to wave-driven runup, which drives beach erosion and overtopping events, is essential for building coastal resilience. Unfortunately, the accuracy of hindcast and forecast models is largely limited by the difficulty of collecting a sufficient quantity of quality validation data.

Runup model validation requires accurate observations of nearshore waves, surf zone bathymetry, wave runup, and the

subaerial beach. Methods for obtaining these observations have advanced rapidly in recent years. In situ surf zone bathymetry surveys are still labor-intensive and involve using a global navigation satellite system (GNSS)-equipped push-dolly, sonar Jet Ski, ATV, or amphibious vehicle (e.g., Ludka et al. 2019; Smith et al. 2017; Turner et al. 2016b; and others). The resources required limit frequency and spatial coverage, particularly during large wave events. In situ observations of wave runup include runup wires (Holman and Guza 1984; Holland et al. 1995) and buried pressure sensors, which can also measure nearshore waves (e.g., Raubenheimer et al. 1998). These are costly to maintain and not easily moved once deployed. Remote observations of nearshore processes for model validation have historically been based on video techniques (e.g., Holman et al. 2013), with the more recent addition of lidar and radar (Brodie et al. 2015; Blenkinsopp et al. 2010; Almeida et al. 2013; Turner et al. 2016b; Vousedoukas et al. 2018; Honegger et al. 2019; and others).

Lidar measurements can provide accurate and highly resolved spatial and temporal elevation measurements of both the water and beach surfaces spanning the swash and surf zones. Brodie et al. (2015) found good agreement ($r^2 > 0.85$) in wave setup and significant wave heights across the surf zone between a dune-mounted surf zone-scanning lidar and buried pressure sensors. Blenkinsopp et al. (2010) likewise found rms errors of less than 4 cm in the swash zone when comparing a platform-mounted lidar to an alongshore transect of altimeters. Using a similar lidar setup, Almeida et al. (2013) compared lidar

^o Denotes content that is immediately available upon publication as open access.

^o Supplemental information related to this paper is available at the Journals Online website: <https://doi.org/10.1175/JTECH-D-21-0027.s1>.

Corresponding author: Julia W. Fiedler, jfiedler@ucsd.edu

DOI: 10.1175/JTECH-D-21-0027.1

© 2021 American Meteorological Society. For information regarding reuse of this content and general copyright information, consult the AMS Copyright Policy (www.ametsoc.org/PUBSReuseLicenses).

to video measurements of storm wave (significant wave height $H_s = 2.5$ m) runup on a gravel beach and found relatively good agreement ($r^2 = 0.7$).

Unlike video methods, lidar can accurately measure wave shape and runup depth. Model parameterizations of wave runup are commonly based on video analyses (e.g., Stockdon et al. 2006), but because video techniques often lack coincidentally collected bathymetry, the estimates of runup depth, or tongue thickness, are subject to error on rapidly changing subaerial beaches (e.g., Voudoukas et al. 2014). For example, Almeida et al. (2013) found the vertical differences between video and lidar-derived runup measurements sometimes exceeded 0.5 m. Lidar can continuously measure the subaerial foreshore elevation when waves recede and the water surface when waves advance. Careful differencing of the two gives depth (e.g., Blenkinsopp et al. 2010; Brodie et al. 2015). Full-depth measurements of the runup tongue make it possible to choose a threshold depth for runup parameterizations, allowing for model-like sensitivity analyses (e.g., Stockdon et al. 2014). The accurate water surface elevation measurements also allow quantification of complex surf-zone processes like bore collapse (Bergsma et al. 2019). In addition, lidar-observed wave transformations can be used for bathymetric inversions in the surf zone (e.g., Martins et al. 2018), where video-based inversion techniques tend to fail. This is because accurate wave shape and height measurements are necessary for corrections to linear theory in the depth-inversion algorithms.

In the coastal geosciences, small aerial drones equipped with cameras are increasingly used to study coastal morphology and ocean waves. Coastal locations do not always have stable locations to erect a tower or for unhindered vehicle access. Drones offer altitude and field-of-view advantages. Using a drone with real-time kinematic (RTK)-GNSS technology, Turner et al. (2016a) found structure from motion (SfM) photogrammetry techniques to be comparable in accuracy to traditional ground-based GNSS terrestrial beach survey methods. Holman et al. (2017) proposed that video from a hovering drone can be used as a remote alternative to fixed Argus camera systems to observe wave runup. Brodie et al. (2019) used a multicamera system to combine SfM processing with a video-based wave speed inversion (cBathy; Holman et al. 2013) algorithm, producing a complete bathymetric and topographic dataset. However, photo and video techniques for measuring waves and runup, whether from a drone or fixed mount, still suffer from the fundamental difficulty of extracting a vertical coordinate on time scales of seconds to minutes.

Lidar-equipped drones are currently used for numerous applications (e.g., archaeology, forestry, mining) including coastal surveying. Lidar active-sensing payloads are more costly than passive-sensing cameras but excel in situations where SfM and camera-based techniques are inadequate. Example use cases are scanning at night, resolving fine features like tree branches and power lines, and mapping terrain below tree canopies in heavily vegetated areas (Lin et al. 2011; Wallace et al. 2012). Lidar-equipped drones are also used for 3D mapping of hazardous environments that are inaccessible such as glaciers, cliffs, and landslides, and for disaster response.

Advancements in drone, lidar, and inertial measurement technology also make lidar wave measurements from a drone possible (Huang et al. 2018), providing increased resolution and vertical accuracy compared with video techniques in areas ill equipped for tower-mounted lidar observations. Here we expand on this new application and present a methodology to observe the surf and swash zone using a drone-mounted lidar developed during a pilot experiment that took place in winter 2019/20. Lidar observations and analysis of waves, subaqueous bathymetry, and wave runup collected during two days with varying surf zone width and incident waves conditions are compared to concurrent measurements from buried pressure sensors, a stationary truck-mounted terrestrial lidar, and bathymetry measurements collected with traditional ground measurement techniques (Jet Ski, dolly, ATV GNSS).

2. Field site

The study was conducted at Torrey Pines State Beach in San Diego, California. The gently sloping mixed cobble and sand beach was instrumented with a transect of six buried pressure sensors extending from the cobble-covered upper beach to ~ 110 m offshore. A drone-mounted lidar hovered at 20 m above the water roughly 40 m offshore, and a truck-mounted terrestrial lidar (elevation 6.3 m, NAVD88) parked on an elevated road above the back beach (Fig. 1). Data were collected during high tide [\sim mean higher high water (MHHW), 1.57-m NAVD88] from 1800 to 1924 UTC 14 December 2020 (four 17-min hovers, D1–4) to 1700–1920 UTC 24 February 2020 (five 17-min hovers, F1–5). In December, large offshore waves ($H_s = 2.2$ m, 16-s peak period, measured at the National Data Buoy Center station 46225 in 525-m water depth 12 km due east of the study site) produced a surf zone width in excess of 180 m, extending past the offshore range of both hovering and stationary lidar. In February, smaller offshore waves ($H_s = 0.8$ m, peak period = 15 s) began breaking between $-80 < x < -55$ m, producing a ~ 50 -m-wide surf zone. Winds, as measured by the National Oceanic and Atmospheric Administration (NOAA) station 9410230, which is 6.5 km south of the study site, were light ($< 2 \text{ m s}^{-1}$) with variable direction for the December collection, and light and onshore for the February collection. Bathymetry measurements were obtained with a suite of acoustic and GNSS-RTK-equipped instruments [i.e., Jet Ski, push-dolly, and ATV; see Ludka et al. (2019) for methods] 3–4 days before and after each hover collection.

3. Instrumentation and data

a. Drone system and payload

The drone payload is a Phoenix Lidar Systems (PLS) miniRANGER LITE. The miniRANGER LITE system consists of a 905-nm Riegl miniVUX-1UAV lidar, a proprietary PLS AIR NavBox, dual GNSS antennas mounted on a 2 m baseline carbon fiber boom, and removable dual Sony A600 Lite cameras. The miniRANGER AIR NavBox integrates the inertial measurement unit (IMU), data storage, CPU, Wi-Fi telemetry, power supply, and I/O components necessary for collecting survey-grade data. The payload was mounted on a

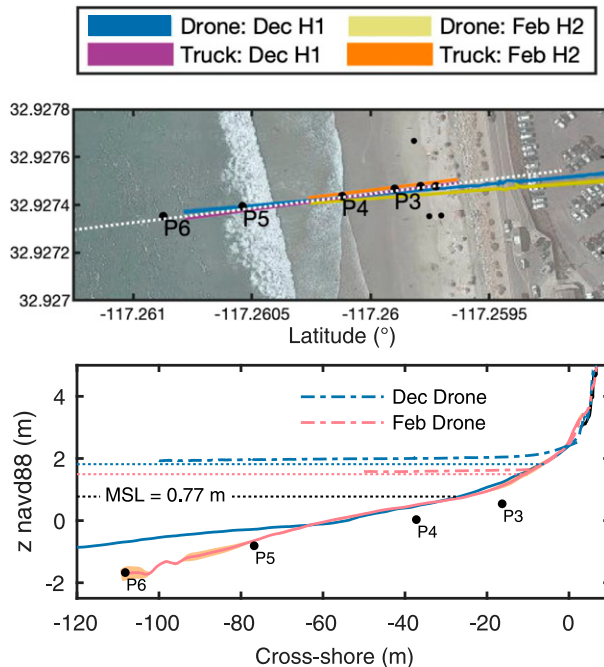


FIG. 1. Overview of study site at Torrey Pines State Beach. (top) An aerial view of the lidar collections from hover on 1 December (D1) and hover 2 on February (F2) from the drone (blue and yellow, respectively) and truck (purple and orange, respectively), with the white dotted line showing the orientation of the local coordinate frame relative to the coast. The width of each lidar line spans four standard deviations of the local alongshore coordinate. (bottom) A transect of buried pressure sensors (black dots) extends from the back beach to the surf zone. Bathymetry during the two collections on 14 Dec 2019 and 24 Feb 2020 are shown with the solid blue and red lines, respectively. Shaded areas indicate elevation differences between two surveys collected prior to and after each collection, spanning approximately 1 week. Dotted lines represent the approximate tide levels, derived from 6-min average records at the nearby La Jolla tide gauge for 24 Feb (red) and 14 Dec (blue) collections. The dotted black line indicates mean sea level at the La Jolla tide gauge. Dashed lines are an example 17-min average sea level surface from the unfiltered lidar time series (here, hover 1 is December and hover 2 is 2 February).

DJI M600 Pro hexacopter (Fig. 2a). The drone hover time was a primary consideration, with the goal of maintaining position for at least 17 min, a record length commonly used in wave runup analysis with video systems (e.g., Brodie et al. 2015; Holman et al. 2017). The DJI M600 Pro platform with extended life batteries (TB48S, 6S LiPo, 6×5700 mAh; 129.96 Wh) weighed 10 kg and with the 4.5-kg lidar payload had an all-up weight of 14.5 kg, allowing for 21-min flights, including time for takeoff, landing, transit, and kinematic alignment maneuvers.

The M600 Pro drone is flown using a remote controller connected to an iPad Pro running either the Litchi iOS app for automated waypoint flight or DJI-GO for manual flight. For the hover flights at Torrey Pines, the preprogrammed hovering waypoint was located directly above a surf zone pressure sensor (P4, Fig. 1). The drone horizontal hovering accuracy with the DJI A3 Pro Flight Controller module GNSS

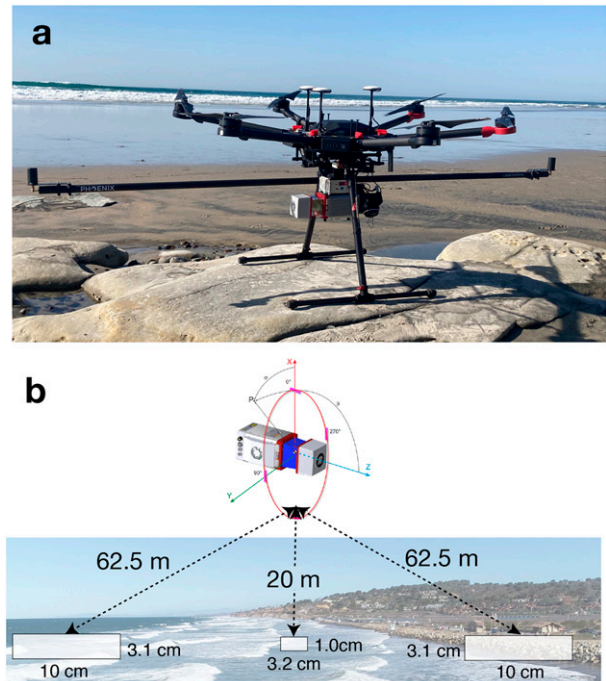


FIG. 2. Platform and laser footprint. (a) DJI M600 Pro hexacopter with a Riegl miniVUX-1UAV. (b) The laser beam footprint of the hovering lidar scanner increases with distance from the drone due to divergence. The maximum 10-cm cross-shore bin size used for resolving runup is at a range of 62.5 m.

is approximately 3 m. The drone heading while hovering was also programmed through the Litchi app for repeatability, with the nose of the aircraft pointing in the alongshore direction so the scanner was oriented for cross-shore scanning.

The payload is remotely controlled separately from the drone via a Wi-Fi link to a notebook PC running Windows 10 OS and PLS Spatial Explorer version 5.0.4. The PLS software displays real-time payload data and telemetry, allowing for real-time QA/QC of the data, as well as remote on-off toggling of the sensors (see online supplemental figure for hardware and software details). The miniRANGER LITE system and drone are available off the shelf but include a few modifications and upgrades to ensure accurate results for stationary hovering, increased flight time, and rapid deployment for repeat flights.

The Riegl miniVUX-1 lidar scanner was chosen for its combination of small form factor, optimal laser wavelength, linear scan pattern, low beam divergence factor, and high angular resolution compared with other sensors on the market at the time of purchase. The scanner uses a single laser that rotates 360° and makes 100 000 measurements per second (100 kHz). While the programmable scan, or spin, rate of the instrument ranges from 10 to 100 lines per second, we chose the lowest speed setting to achieve the best angular resolution. We conducted an initial hovering altitude test at 20, 30, and 40 m above sea level along a cross-shore transect. A flight altitude of 20 m produced the most points per meter per second from the lidar. At this altitude, the 1.6-mrad beam divergence corresponds to a

rectangular laser footprint of $3.2 \text{ cm} \times 1.0 \text{ cm}$ (3.2 cm^2) directly under the lidar (Fig. 2b), with over 680 returns per meter per second. The divergence increases the footprint to $10 \text{ cm} \times 3.1 \text{ cm}$ (31 cm^2) at a 62.5-m range from the lidar, with roughly 70 returns per meter per second.

Mobile lidar systems are designed to scan stationary targets while the lidar unit is moving through space (kinematic). Obtaining wave runup time series data, however, requires the drone to remain stationary while measuring moving targets. When stationary, the onboard microelectromechanical system (MEMs) IMUs commonly used on drones due to lower cost and weight are subject to drift. This is a concern especially with respect to heading, as hovering may not provide sufficient dynamics for constraining IMU drift. To overcome this, we used an upgraded IMU (PLS IMU-27, a Sensoror STIM300, 125 Hz sampling) with a custom 2-m dual baseline antenna setup mounted on carbon fiber booms. The dual-antenna receiver provided GNSS positioning (Novatel OEM7720, 1-Hz sampling) at 2-m antenna separation, with heading rmse of 0.1° . The primary antenna is for positioning, and the secondary antenna is used for position-differenced heading. Real-time data precision for the dual antenna system is calculated by the onboard NovAtel SPAN firmware, and postprocessed with NovAtel Inertial Explorer software. Additionally, following manufacturer training, we performed kinematic alignment maneuvers to initialize the inertial navigation system for each flight. These consisted of flying a straight line for 10 s at a speed $> 5 \text{ m s}^{-1}$ as well as a figure-eight pattern before and after each hover.

With a team of three people, the lidar drone can be set up and deployed within 30 min of arrival on site. Downtime between each 21-min flight to swap batteries and resume data collection was reduced to 5 min. While the drone is on the ground, the system uses an external LiPo battery for ground power to keep the lidar and GNSS system running without interruption. Care was taken to avoid blocking GNSS antennas.

b. Terrestrial truck lidar

A terrestrial lidar (1550-nm Riegl VMZ-2000) was mounted on a pickup truck equipped with a dual boom GPS antenna, and an Applanix AP-20 IMU. While the truck is outfitted to be a mobile system for use in large-scale beach and cliff monitoring (Young et al. 2021), we adjusted the data acquisition and processing methods to replicate a stable platform. Each wave scanning collection period commenced with a stationary 360° rotational site scan used for georeferencing, with the truck positioned perpendicular to the survey transect (Fig. 1). Subsequent wave scans were taken with the lidar fixed on the transect at 100 kHz (10 lines per second). The lidar operators remained outside the vehicle to reduce unnecessary scanner movement, and an external generator supplied power to the scanner and acquisition laptop to eliminate potential vibrations from the truck engine.

c. Data processing

Drone lidar trajectory data were postprocessed using NovAtel Waypoint Inertial Explorer (v 8.80) software. GNSS rover data

from the drone was processed using base data from a NOAA Continuously Operating Reference Station (CORS) site located 10 km away (SIO5). Laser data were georectified and exported to LAS format using PLS Spatial Explorer (v 5.0.4) software. Terrestrial lidar data were postprocessed and georectified using Riegl RiScanPro software to match planes to a control site survey. Each drone and terrestrial wave scan was rotated into the local coordinate system and gridded by 10 cm into an (x, z, t) matrix following Brodie et al. (2015), whereby each single line scan was separated in time using the scan angle of the lidar, corresponding to a ~ 0.1 -s time step (10 lps). Both hovering and terrestrial data matrices were then synced and interpolated to the same 0.1-s time grid for direct comparison. Slight along-shore differences due to differing heading angles between each hover and $y = 0$ are neglected in this processing schema (see section 9 for a discussion of potential errors). Reflectance values less than -27 dB in the terrestrial data, manually classified as sea spray, were removed. We further stabilize the drone data by applying a global vertical correction corresponding to the vertical fluctuations ($\pm 5 \text{ cm}$) observed at a 5 m-wide stable location in the back beach.

Buried pressure sensors (battery-powered Paroscientific model 245A-102 combined with custom electronics), sampling at 2 Hz on near hourly intervals (7167 samples at the start of each hour), were corrected to the seabed following linear theory for burial in completely saturated sand (Yamamoto et al. 1978; Raubenheimer et al. 1998) and surface corrected using a nonlinear weakly dispersive method for the water column (Bonneton et al. 2018). Data were first low-pass filtered with a frequency cutoff 0.33 Hz (3-s waves) to ensure smooth time derivatives in the surface correction. A hard cutoff of 0.5 Hz (2-s waves) was used in the burial correction to avoid overamplification of high-frequency signals. Significant wave heights for both pressure sensors and lidar data are calculated using the surface elevation time series, or $H_s = 4\sigma_\eta = 4\sqrt{\int S_{\eta\eta}}$, where $S_{\eta\eta}$ is the surface elevation spectrum.

4. Vertical precision of the hovering lidar data

Drone lidar data are noisier in the vertical than the terrestrial (truck) lidar. Alongshore elevation variations due to horizontal drifting of the drone may show up as vertical movement in the lidar data. In addition, there are the inherent accuracy limitations of kinematic GNSS solutions. Trajectory data for hovers 1, 3, and 4 in December (D1, 3, 4), and hovers 2–5 in February (F2–5) were considered of a quality sufficient for further processing. We rejected D2 and F1 due to large irreconcilable vertical offsets ($\sim 0.5 \text{ m}$) in the scan data, which we attribute to poor satellite reception.

Slightly larger alongshore scan footprints are observed in the February hovers ($\bar{\sigma}_y = 45.8 \text{ cm}$ in December vs $\bar{\sigma}_y = 61.2 \text{ cm}$ in February at $x = 45\text{--}50 \text{ m}$ and $\bar{\sigma}_y = 34.7 \text{ cm}$ vs $\bar{\sigma}_y = 41.0 \text{ cm}$ at $x = 0\text{--}2 \text{ m}$). In contrast, the alongshore width of the terrestrial lidar collection is much smaller, with a standard alongshore deviation of near 0.5 cm at the foreshore. Mean vertical offsets between the hovering and terrestrial sources are unsteady (maximum of 6 cm on the upper beach), which we ascribe to alongshore differences between the two lidar transects (Fig. 1a).

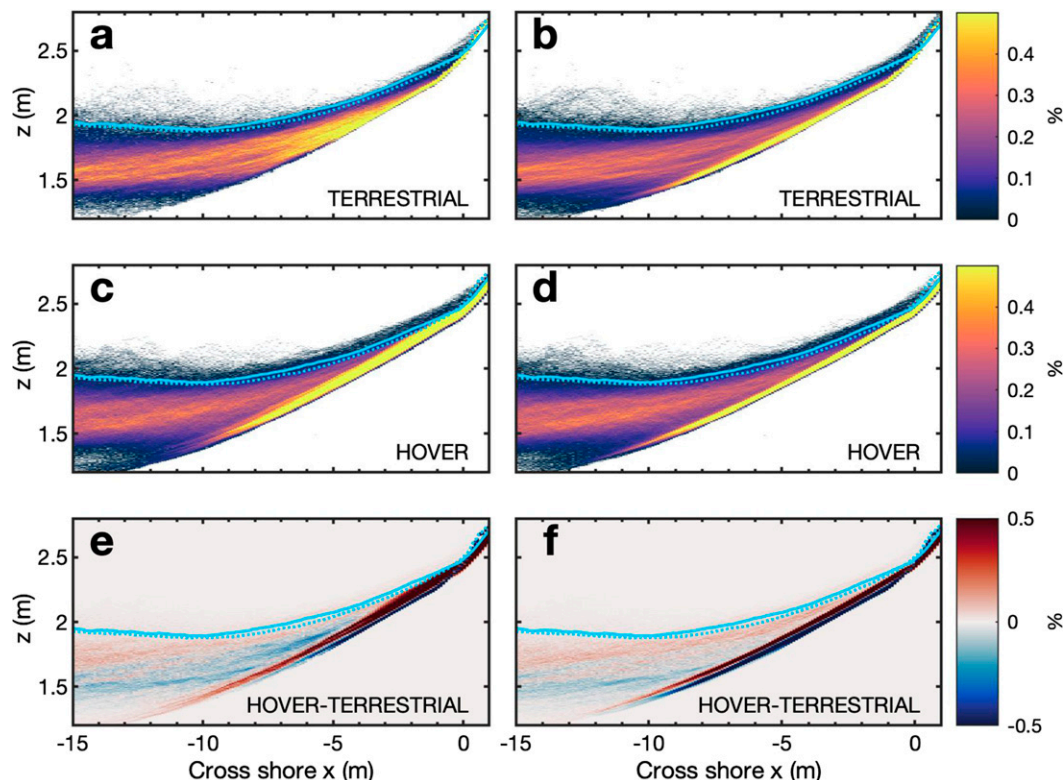


FIG. 3. Histograms of lidar elevation data for hover 2 on 24 Feb 2020 (F2). Histograms (% of total counts) of the swash zone for F2 as seen by the (a),(b) terrestrial lidar, (c),(d) drone lidar, and (e),(f) the difference between the two. (a),(c),(e) Histograms of the initial gridded data reveal (e) strong differences between the platforms. (b),(d),(f) The terrestrial and hover data are interpolated to fill data gaps, and the global vertical fluctuations (± 5 cm) in the hover data are removed. The 98th percentile of elevation using the terrestrial (dotted) and hovering (solid) lidar is plotted in light blue for each grid point.

These vertical errors are confounded by a slight increasing vertical offset ($\sim 2 \text{ cm h}^{-1}$) in time between terrestrial lidar scans observed in the December collection, which we attribute to a scanner coordinate shift in the terrestrial control scan. The observed terrestrial scanner drift did not occur in February.

The differences in the precision of the vertical foreshore location between a stable and hovering platform are apparent in the histograms, or percent of total counts, of the vertical measurement at each cross-shore point for both lidar systems (Fig. 3). For example, in the upper beach, the drone sees higher noise with a vertical standard deviation of 2.5 cm, compared to the terrestrial lidar of 0.8 cm as shown by slightly “thicker” foreshore due to noise from hovering (yellow high-density areas, Fig. 3b). Note that this is also an effect of the color limit, which saturates at 0.5% to highlight the swash zone. No obvious sources stand out for the source of these fluctuations; there is no significant coherence with the heading, pitch, roll, or horizontal drone location, and no significant frequencies at which they oscillate. Removing the low-frequency vertical fluctuations (± 5 cm) in the drone reduces the standard deviation of the drone to 1.7 cm and increases the coherence between stationary and drone lidar returns at all cross-shore points (Fig. 4).

The vertical standard deviation at a known stable location (Torrey Pines parking lot, $x = 45\text{--}50$ m) is likewise reduced from an average of 2.3 to 1.1 cm for all hovers.

5. Spatial coverage of lidar systems

Despite identical settings, we found significant differences in the laser returns between the two days of data collection (Fig. 5). In February with small waves ($H_s = 0.8$ m) and light onshore wind, the smooth mirror-like surface seaward of the narrow surf zone drastically reduced lidar returns for $x < -50$ m. We attribute the lower number of laser returns to absorption and specular reflection. In contrast, in December ($H_s = 2.2$ m) the surf zone extended more than 180 m offshore, and usable data were obtained to $x = -120$ m. We attribute the higher number of laser returns during the December experiment to greater diffuse reflectivity of the water surface. Higher H_s increased the surf zone width and amount of whitewater (aerated water) in the drone’s field of view. Whitewater scatters the laser more diffusely, yielding a greater number of surface returns farther offshore of the drone’s position.

The density of uninterpolated gridded laser returns between the hovering and terrestrial lidars is also notable. Because of

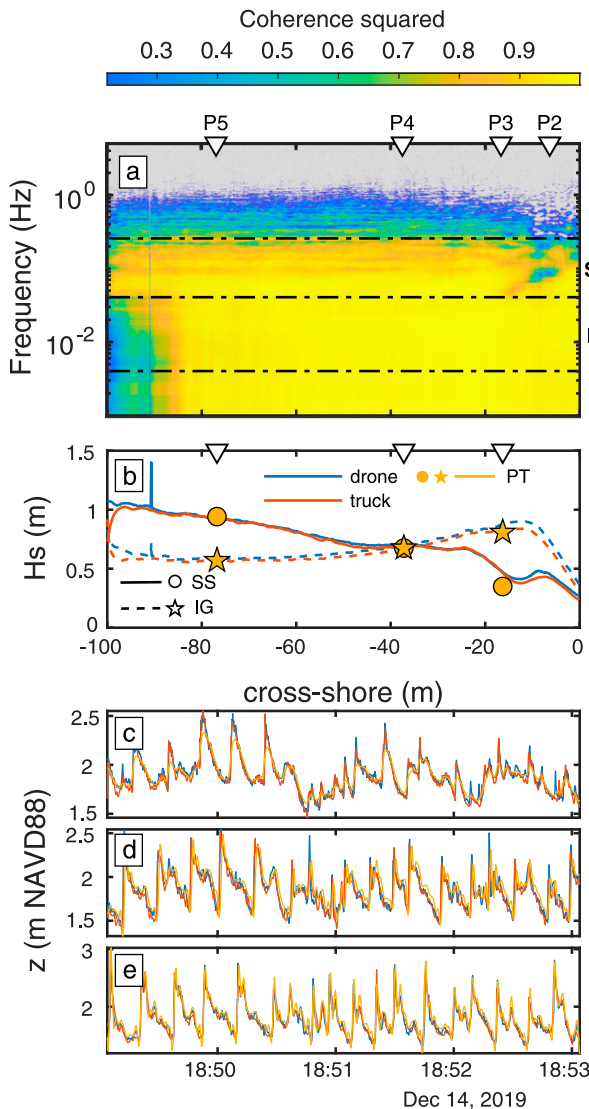


FIG. 4. Instrument comparisons for December hover 3. (a) Squared coherence (between the interpolated drone and terrestrial lidar) vs cross-shore distance. Sea-swell and infragravity bands are bounded by dashed black lines. Only squared coherence above the 95% significance level are shown. (b) Significant wave height in the cross-shore for the infragravity (dashed and stars) and sea-swell bands (solid and circles). Pressure sensor P2 is intermittently covered with water in the swash zone and is not shown. (c)–(e) Example 4-min elevation time series of the unfiltered 10-Hz drone lidar, terrestrial lidar, and surface-corrected pressure sensors (blue, red, and yellow, respectively) at P3 [$x = -16$ m, (c)], P4 [$x = -37$ m, (d)] and P5 [$x = -77$ m, (e)].

the low grazing angle of the terrestrial lidar, the back of the waves were often shadowed, requiring interpolation in the final gridded data product. This is readily seen in the large wave at the 1-min mark of the D3 time series (Figs. 5a,b, arrow). Data returns on the upper beach are likewise sparse, due to shadowing from the back beach boulders and specular reflection on the slick foreshore.

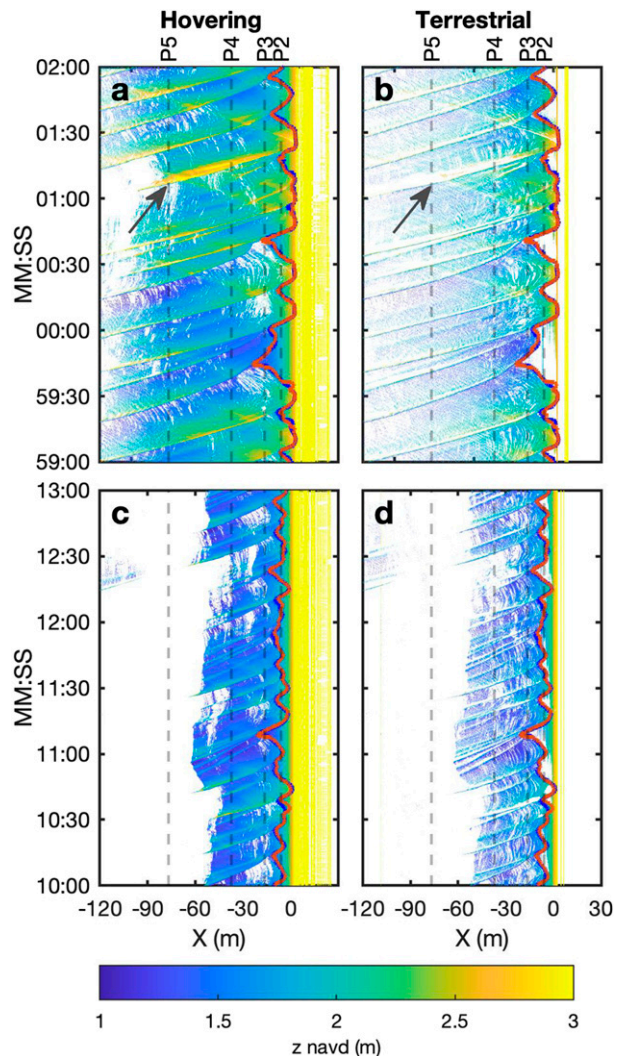


FIG. 5. A 3-min subsample of 5-cm gridded and uninterpolated lidar surface elevation time stack from the (left) drone and (right) terrestrial lidar on collection (a),(b) D3 and (c),(d) F3. The 5-cm-threshold runoff line (discussed in section 8) is plotted for the terrestrial (red) and hovering (blue) data for reference. The drone occasionally sees larger swash excursions (rundown and runup), which may lead to larger statistical measures of incident swash. Cross-shore locations of pressure sensors are denoted in dashed gray lines.

6. Surf zone wave measurements

Surf zone wave measurements agree well between all three fully processed measurement systems (Fig. 4), with the largest differences in higher frequencies. Discrepancies between the two lidar collection systems occur at the offshore edge of the cross-shore domain and near the swash zone, where more interpolation is required due to sparse lidar returns (Fig. 4a). Significant wave heights (H_s) agree well in both the infragravity band (IG; 25–250-s period) and sea-swell band (SS; 4–25-s period, Fig. 4b). As noted by Blenkinsopp et al. (2010), Brodie et al. (2015), and others, lidar data should be better able to capture the nonlinear surf zone, as both lidars sample at a

higher frequency than the buried pressure sensors (10 vs 2 Hz). Using the nonlinear surface correction method, however, we find good agreement in the bulk surf zone statistics between the lidars and the surf zone pressure transducers (PTs) (P4, P5), with average normalized rms differences (NRMSD) less than 3% for both IG and SS frequency band significant wave heights in the December hovers. During the February hovers, only P4 was in the surf zone, with slightly higher averaged normalized rms differences of less than 5%, corresponding a 2-cm difference in wave heights. Relative variance differences for all frequencies are on average 7% for the December hovers, and 12% for February, larger than the 5% found by Martins et al. (2020). The larger differences may be attributable to the substrate in which the sensors are buried, lack of sensitivity to water aeration (seafoam), lower-frequency sampling of the PTs, and for February, much smaller waves in the inner surf zone. Note we have excluded P3 from this comparison. While IG significant wave heights agree (NRMSD < 8%), the PT is at the offshore edge of the swash zone, where the assumption of full saturation of the mixed cobble and sand beach may not be valid in the PT burial correction. This leads to an underestimation of SS wave heights on the order of 25% (see Fig. 4). In addition, a small bias is observed (≤ 5 cm) between the pressure sensors and the lidar systems which we attribute to GNSS and/or measurement error.

7. Surf zone bathymetry

Remote surf zone bathymetry estimates are often obtained via optical sensors (e.g., Argus cameras; Yoo et al. 2011; Catálan and Haller 2008; Brodie et al. 2018), but have recently expanded to radar (Honegger et al. 2019) and lidar measurements (Martins et al. 2018). The depth-inversion algorithms generally begin with a direct estimation of wave celerity c or wavenumber–frequency pair (k, f) in space by either tracking individual wave crests in the space–time domain via pixel intensity (Yoo et al. 2011) or local maximum elevation (Tissier et al. 2015), or by Fourier transforming intensity values $I(x, t)$ into wavenumber–frequency space (cBathy algorithm; Holman et al. 2013). From there, depth is solved for using the phase speed $c = \omega/k$, with $\omega^2 = gk \tanh(kh)$, where ω is the radial frequency ($2\pi f$) and h is water depth. In shallow water, the dispersion relationship reduces the expected phase speed to $c = \sqrt{gh}$, greatly simplifying the inversion. In the surf zone, however, the accuracy of linear theory often fails as waves break and the ratio of wave height to water depth increases. For these reasons, a k – ω approach can also magnify errors in shallow water. Corrections to surf zone celerity for bores, breaking waves, and rollers (e.g., Hedges 1976; Booij 1981; Thornton and Guza 1982; and others) have been shown to improve bathymetry estimations in this often highly nonlinear region (e.g., Honegger et al. 2019; Tissier et al. 2015; Martins et al. 2018).

Here we estimate celerity following Tissier et al. (2015) for tracking wave crests. The elevation data are gridded in $\eta(x, t)$ coordinates. Data grids are truncated in the cross-shore to avoid overinterpolation of sparse time series. Peaks along the offshore edge are identified as wave crests. Once a crest is found, a 5 m search window is established in the cross-shore

direction, such that $x_i - 2.5 < x_i < x_i + 2.5$ m, following Martins et al. (2018). For each time step, the maximum elevation within that search window marks the location of the wave crest. The procedure is repeated for each subsequent time step until a forward-propagating wave crest can no longer be identified (see Fig. 6b, red circles). Wave crests with unphysical shoreward progress (i.e., leaps or halts) are also likewise discarded. For each wave and cross-shore location, we apply a linear regression over a moving cross-shore window to establish the wave speed $c = dx/dt$. The size of this window varies in x , from $\Delta x = 10$ m at $x = -100$ m to $\Delta x = 1$ m at $x = -10$ m, to account for more rapidly changing wave speeds nearer to shore. We solve for depth using linear theory, $h = c^2/g$, and take the median h over all waves for each cross-shore location. Note that there is no tidal dependence in this method, in contrast with traditional video techniques which require a vertical datum. Here, depth is calculated directly from the lidar-measured mean sea surface elevation.

For depth inversions in the surf zone, linear phase speed is replaced with the commonly used Booij (1981) bore-theory model (e.g., Catálan and Haller 2008; Tissier et al. 2015; Martins et al. 2018),

$$c^2 = \frac{g}{k} \tanh[k(h + H/2)], \quad (1)$$

where H is crest-to-trough wave height. We estimated H as the difference in maximum (peak) and minimum (trough) of sea surface heights on each wave face for each time step and cross-shore location (Fig. 6b). Depth is then calculated as $h = \overline{c^2/g} - H/2$, where the overbar denotes the time median assuming a shallow-water simplification.

Averaged crest-tracked inverted bathymetries compare well to in situ measurements, collected with traditional ground-based GNSS-RTK techniques 3–4 days before and after the hovers (Fig. 6). As noted by previous authors, linear inversions (red lines, Figs. 6a,c) overpredict water depth as wave breaking increases (e.g., Tissier et al. 2012). Adjusting wave celerity for bores improves the agreement in this shallow region (green lines). The inversions appear to fall off in agreement with in situ data in very shallow water ($h < 0.75$ m), but these cross-shore locations also correspond to the swash zone where the sand is intermittently covered by waves. Here, the ratio of H/h may increase asymptotically (e.g., Sénéchal et al. 2004; Power et al. 2010; Martins et al. 2016), which overamplifies the depth inversion. To account for this, a reasonable average bathymetric profile can be extracted using the inversions with bore correction, and the lidar-observed sand elevation during rundown events.

While the inversion results for the terrestrial and drone lidars are similar, the comparison is limited by the sparseness of the terrestrial lidar data. At distance, raw terrestrial elevation data tend to skew lower than the drone data, potentially leading to a smoother interpolated sea surface (see section 8 for interpolation details). The crest-tracking method, which relies only on the location of the wave peak, is generally insensitive to this data sparseness, but still diverges from the drone results near the edge of the interpolated domain (not shown).

The bathymetric inversion assumes the lidar scan alignment and waves are shore-normal. Oblique wave incidence θ increases

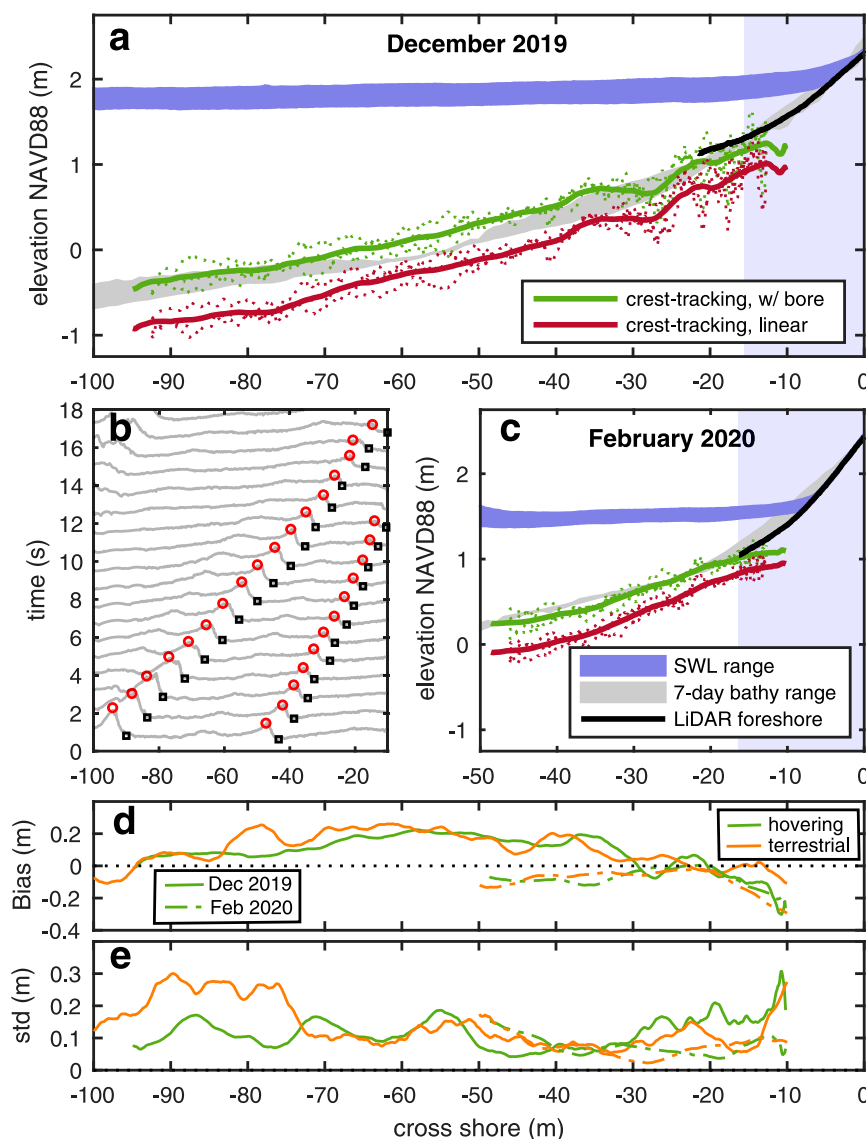


FIG. 6. Mean bathymetry inversions from the drone lidar for the (a) December 2019 ($n = 3$) and (c) February 2020 ($n = 4$) hovers. Gray shaded areas indicate the vertical range of in situ bathymetry collected on the transects in the 7-day window surrounding the hovers. The black line is the hovering lidar-derived foreshore. Blue shaded areas are the mean still-water-level ranges over the hover collection. Wave setup and setdown are necessarily included. The solid red and green lines indicate bathymetry derived with the crest-tracking technique for the linearly derived profile (red) and bore-corrected profile (green) for each day. For visual simplicity, all averages are 8-m moving means. Individual hover results are plotted with dotted lines. The swash zone, defined as two standard deviations about the mean horizontal runup, is marked in light blue. (b) A subset of example waves used in the December 2019 inversion, plotted at 0.5-s intervals. The crest-tracking technique follows the wave crests (red circles). Wave troughs, used in the bore correction technique, are denoted by black squares. (d) Bias and (e) standard deviation of the bore-corrected bathymetry inversions and the mean in situ data for the hovering (green) and terrestrial lidar (orange) December (solid) and February (dashed) collections.

the measured speed to $C \cos \theta$. For example, a relatively large local swell angle of 15° only introduces 4% C error. Reflection from the back beach riprap, a strong alongshore current, and energetic infragravity waves and/or bore-bore capture may also

contribute to individual wave speed errors (Tissier et al. 2015). The results for larger waves in December are correspondingly noisier in the inner surf zone than the results in smaller waves in February (Fig. 6).

8. Runup statistics

Estimation of the wave runup limit, here defined as the cross-shore location of 5-cm water depth above the sand, requires a relatively stable foreshore from which to extract the water depth. In a typical terrestrial lidar collection, a “wet” and “dry” time series of all cross-shore points can be obtained by assuming the sand level fluctuation to be much less than that of the moving water surface (Almeida et al. 2013; Brodie et al. 2015). We roughly follow this method, with the caveat that hovering lidar has a larger noise floor. To establish sand levels, and distinguish between sand and water, a 100-s moving minimum is first applied to the data that removes noise and high-frequency sand and water changes. For each time step, this “low-frequency foreshore signal” is spatially smoothed with a cross-shore fifth-order (50 cm) median filter.

The runup toe is the cross-shore location of the intersection between the filtered foreshore and the instantaneous water levels at the 5-cm vertical threshold. A 1-s median filter is then applied to the resulting cross-shore runup line. Data gaps are interpolated with a Laplacian model (D’Errico 2019). The cross-shore location of runup is then transformed to the vertical datum to obtain a vertical runup time series (Fig. 5).

Statistics of wave setup and significant sea-swell (4–25 s) and infragravity (25–250 s) swash are obtained from spectra (Fig. 7). Expected errors of each component are a function of sampling time as well as the strength of the signal, following Elgar (1987). Swash components are statistically similar (within expected error) for all hovers. While still within the expected spectral error margins, drone-derived runup components are, on average, larger than those derived with the terrestrial lidar (Fig. 7). This may be due to the shadowing and/or poor returns on the upper beach from the low look angle of the terrestrial lidar.

The runup threshold chosen here (5 cm) is on the larger end of typical detailed lidar-derived runup studies (e.g., 5 cm; Almeida et al. 2013; and 1.5 cm; Martins et al. 2016; Brodie et al. 2012). The laser footprint of the hovering lidar is 10 cm in the swash zone (Fig. 2b), and thus both lidars are compared at this horizontal resolution. On the upper beach, this grid size corresponds to roughly 3-cm vertical change due to the bed slope, with a maximum 1.7-cm vertical standard deviation. A threshold of 5 cm therefore allows for comparison between the two lidar systems above the expected bed-measurement noise floor.

9. Discussion

Surf zone processes and wave runup are sensitive to surf and swash-zone bathymetry (e.g., Stephens et al. 2011; Gomes da Silva et al. 2020). The depth inversions presented here are ground truthed with Jet Ski and push-dolly bathymetry measurements with a small ($\Delta z < 12$ cm) bias for cross-shore locations outside the swash zone (Fig. 6d). Previous video-derived bathymetry results have shown similar bias, but require shoaling, breaking, and dissipation models with tuning parameters for the observed waves (Yoo et al. 2011). Estimating wave height for the inversion directly from lidar data eliminates the need to tune these model parameters.

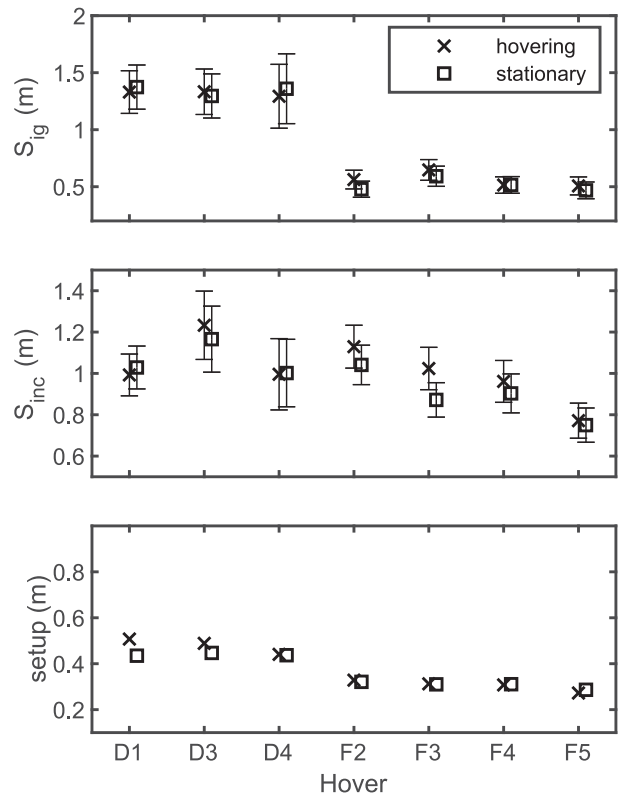


FIG. 7. Observed (seven hovers) bulk runup statistics using the hovering drone lidar and terrestrial truck lidar (crosses and squares, respectively) of (a) IG swash, (b) incident swash, and (c) setup. Error bars on the measurements are from spectral noise only, as instrument error could not be well estimated. Each set of hovers were taken on a falling high tide in December (D) and February (F).

A system incorporating both lidar and Argus-type technology can be used to extend remote survey capabilities and bathymetry inversions; eBathy excels outside the nonlinear breakpoint (e.g., Holman et al. 2013; Brodie et al. 2019), whereas lidar benefits from the increased returns of a reflective surf zone. Additionally, the hovering sUAS is capable of mobile topographic surveys, covering wide swaths of the subaerial beach.

a. Drone limitations

While the hovering platform allows for mobility and enhanced observations in locations logistically difficult for a terrestrial lidar setup, its use is limited by regulations, weather conditions, hover times, and the accuracy of onboard navigational systems. The Federal Aviation Administration (FAA) regulates all drone flights in the United States. The drone used in this study falls under part 107 rules for small (<24.95 kg) uncrewed aircraft systems. Currently, drone operators must maintain part 107 pilot certification and obtain special waivers to fly in controlled airspace or over people. Some localities further regulate drone use. Regulations are constantly evolving and can preclude flights in some cases.

The present drone and payload are not rated to fly in visible moisture, including fog and rain, and as such may require

increased maintenance in coastal environments. Lidar performance is degraded in rain, and current FAA regulations prohibit sUAS flights when visibility is less than 4.8 km or there are low clouds unless the pilot obtains a special waiver. Coastal fog can restrict flights even if the hardware is impervious. The DJI M600 Pro used here has a listed maximum wind speed tolerance of 8 m s^{-1} , but has anecdotally flown successfully in sustained wind speeds of 9 m s^{-1} with gusts to 13 m s^{-1} (fresh-strong breeze on Beaufort wind scale). The lidar payload and dual boom increase the windage of our platform, reducing flight time in windy conditions. In the December deployment ($H_s = 2.2 \text{ m}$), salt crystal deposits formed on the leading edges of the drone propellers. The fans used for air-cooling payload electronics and the electronics are also subject to corrosion.

Hovering time depends on drone and payload weight, power supply/battery capacity, wind, temperature, and humidity. The DJI M600 Pro with upgraded TB48S 150 Wh batteries consistently achieved 17-min hovers and approximately 20-min flight time with moderate temperature and low winds. Landing, swapping batteries, and returning to station took approximately 5 min. Sustained repeat flights are possible when using a portable generator or any power source to recharge batteries. Lighter payloads, improved power systems, and more efficient drones will improve endurance.

The quality of the drone flight controller GNSS and IMU affected its ability to hold position throughout the hover. We observed 3-m alongshore drift, and variable heading angles, due to the drone's movement during the 17-min hovers (not shown). This drift is partially due to separate navigation systems for drone and mounted lidar. An RTK positioning upgrade for the drone's flight controller was available but restrictive, due to reliability concerns and added weight. A more stable and accurate drone heading would also decrease the vertical noise along the cross-shore transect. Real-time headings available from the lidar payload are not linked to the flight control software. Integrating the flight controller and payload navigation systems would reduce these issues and reduce overall weight.

Some hover data (hover 2 in December 2019 and hover 1 in February 2020) were excluded from analysis in this paper, due to large ($\sim 0.5 \text{ m}$) irreconcilable vertical offsets in the scan data. These offsets appear to be caused by the momentary loss of satellite reception. The small antennas/grounding planes on the GNSS boom reduce the overall performance. On some data, lowering the elevation mask from 12° to 10° improved the postprocessed solution substantially. Degradation could also be related to sudden movements of the drone and antenna booms when compensating for wind gusts or maneuvering to a hovering position. The carbon fiber booms are not fully rigid and could be seen flexing at times.

b. Lidar quality

Lidar quality depends on range, water clarity, and grazing angle, among other factors (e.g., [Blenkinsopp et al. 2010](#); [Brodie et al. 2015](#); [Almeida et al. 2013](#)). These quality issues may lead to a trade-off between spatial coverage and the accuracy of more detailed surf and swash zone processes. The initial setup described here is an adequate starting point.

Further tests are needed to optimize hovering elevation and cross-shore location. The lidar cross-shore location alters the laser grazing angle that in turn may affect the quality of laser returns with distance from the drone, and optimal hover elevation and location may be much different for wide and narrow surf zones. With the wide surf zone in December, complete cross-shore coverage may have been provided by additional hovers at different cross-shore locations or elevations. Sun glint, water clarity, and wind magnitude and direction may also affect hover location choice.

Confounding the comparison between the stationary and terrestrial systems are the wavelength differences (905 and 1550 nm) and beam divergence of the two lidar systems. The terrestrial 1550-nm wavelength, normally used for beach and cliff surveys, readily reflects the dry beach, but wet sand reflectively is reduced by roughly 70% ([Wojtanowski et al. 2014](#)). Furthermore, the 905-nm wavelength is almost twice as likely to reflect the wet sand than the 1550-nm wavelength. Accordingly, the 905-nm wavelength more readily reflects off the water surface and wet beach—most notably in the swash zone ([Fig. 5](#)). The beam divergence of the VZ2000, at 0.35 mrad, provides a higher horizontal resolution than the 1.6 mrad of the miniVUX. This may play a role in the apparent data density differences at the outer edges of the cross-shore domain, and limits our horizontal grid spacing to 10 cm for both systems.

Potential errors from drift in the terrestrial lidar (2 cm h^{-1} for the December collection) may persist without the matching planes and retro-reflector targets in the field that enable enhanced hourly coregistration corrections ([O'Dea et al. 2019](#)). February collections included 360° site scans in between wave scans for coregistration, as opposed to using only the first 360° control scene before all flights. We found no significant difference between the methods, likely due to the lack of observed significant drift in February. While further testing is warranted, the method presented here for rapid deployment of a terrestrial lidar for a short period appears sufficient and promising.

10. Conclusions

The hovering drone-mounted lidar allows for mobile and semiremote acquisition of simultaneous beach and wave data, including surf zone wave measurements, bathymetry, and wave runup. The package offers several advantages over traditional monitoring techniques like video cameras and fixed terrestrial lidar platforms, such as use in inaccessible areas and locations without a suitable elevated fixed platform. In addition, the drone and lidar package require no fixed platform fabrication or installation. The acquired data are obtained with a built-in vertical reference frame, negating the need for in situ GPS beach surveys, instruments, or a local tide gauge in bathymetry inversion estimates. Unlike cameras, however, the tested drone lidar with a single beam source cannot monitor more than one cross-shore transect concurrently. Additionally, poor lidar returns in calm glassy conditions remain an issue. Complementary systems (cameras and lidar) would improve our remote sensing capacity.

For the present application, the drone system is preferred over the terrestrial method due to the higher look angle and

increased data returns, despite the limited flight times. While the vertical accuracy was slightly diminished, careful quality checks could be automated with the inclusion of a control surface to reduce the vertical fluctuations in the hovering lidar data.

Acknowledgments. This research was supported by the U.S. Army Corps of Engineers (W912HZ192) and California Department of Parks and Recreation (C19E0026). Bob Guza provided helpful discussion and comments. Thanks to Brian Woodward and the CPG field crew including Lucian Parry, Kent Smith, Greg Boyd, and Shane Finnerty. Michele Okiihiro, Bonnie Ludka, and Hiro Matsumoto assisted with experiment logistics. Cassandra Henderson, Athina Lange, Mika Siegelman, and Mele Johnson assisted with field data collection. Thanks also to Ben Adler from Phoenix Lidar Systems for providing technical guidance. Bill O'Reilly provided gridded bathymetric data along MOP 582 that aided in improved sand burial corrections. Last, thanks to the anonymous reviewers who made valuable contributions to improve the manuscript.

Data availability statement. Gridded and processed lidar and pressure data created and used in this study are available from the UC San Diego Library Digital Collections at <https://doi.org/10.6075/J04F1P9V>. Offshore wind and wave data were obtained from NOAA at https://www.ndbc.noaa.gov/station_page.php?station=46225 and <https://tidesandcurrents.noaa.gov/met.html?id=9410230>.

REFERENCES

- Almeida, L. P., G. Masselink, P. Russell, M. Davidson, T. Poate, R. McCall, C. Blenkinsopp, and I. Turner, 2013: Observations of the swash zone on a gravel beach during a storm using a laser-scanner (lidar). *J. Coastal Res.*, **65**, 636–641, <https://doi.org/10.2112/SI65-108.1>.
- Bergsma, E. W., C. E. Blenkinsopp, K. Martins, R. Almar, and L. P. M. de Almeida, 2019: Bore collapse and wave run-up on a sandy beach. *Cont. Shelf Res.*, **174**, 132–139, <https://doi.org/10.1016/j.csr.2019.01.009>.
- Blenkinsopp, C. E., M. A. Mole, I. L. Turner, and W. L. Peirson, 2010: Measurements of the time-varying free-surface profile across the swash zone obtained using an industrial lidar. *Coastal Eng.*, **57**, 1059–1065, <https://doi.org/10.1016/j.coastaleng.2010.07.001>.
- Bonneton, P., D. Lannes, K. Martins, and H. Michallet, 2018: A nonlinear weakly dispersive method for recovering the elevation of irrotational surface waves from pressure measurements. *Coastal Eng.*, **138**, 1–8, <https://doi.org/10.1016/j.coastaleng.2018.04.005>.
- Booij, N., 1981: Gravity waves on water with non-uniform depth and current. Ph.D. thesis, Technical University of Delft, 139 pp., <https://repository.tudelft.nl/islandora/object/uuid%3A05f9b2b1-b237-491f-927a-2a470e0808f3>.
- Brodie, K. L., R. K. Slocum, and J. E. McNinch, 2012: New insights into the physical drivers of wave runup from a continuously operating terrestrial laser scanner. *2012 OCEANS*, Hampton Roads, VA, IEEE, <https://doi.org/10.1109/OCEANS.2012.6404955>.
- , B. Raubenheimer, S. Elgar, R. K. Slocum, and J. E. McNinch, 2015: Lidar and pressure measurements of inner-surfzone waves and setup. *J. Atmos. Oceanic Technol.*, **32**, 1945–1959, <https://doi.org/10.1175/JTECH-D-14-00222.1>.
- , M. L. Palmsten, T. J. Hesser, P. J. Dickhudt, B. Raubenheimer, H. Ladner, and S. Elgar, 2018: Evaluation of video-based linear depth inversion performance and applications using altimeters and hydrographic surveys in a wide range of environmental conditions. *Coastal Eng.*, **136**, 147–160, <https://doi.org/10.1016/j.coastaleng.2018.01.003>.
- , B. L. Bruder, R. K. Slocum, and N. J. Spore, 2019: Simultaneous mapping of coastal topography and bathymetry from a light-weight multicamera UAS. *IEEE Trans. Geosci. Remote Sens.*, **57**, 6844–6864, <https://doi.org/10.1109/TGRS.2019.2909026>.
- Catalán, P. A., and M. C. Haller, 2008: Remote sensing of breaking wave phase speeds with application to non-linear depth inversions. *Coastal Eng.*, **55**, 93–111, <https://doi.org/10.1016/j.coastaleng.2007.09.010>.
- D'Errico, J., 2019: inpaint_nans. MathWorks, <https://www.mathworks.com/matlabcentral/fileexchange/4551-inpaint-nans>.
- Elgar, S., 1987: Bias of effective degrees of freedom of a spectrum. *J. Waterw. Port Coastal Ocean Eng.*, **113**, 77–82, [https://doi.org/10.1061/\(ASCE\)0733-950X\(1987\)113:1\(77\)](https://doi.org/10.1061/(ASCE)0733-950X(1987)113:1(77)).
- Gomes da Silva, P., G. Coco, R. Garnier, and A. H. Klein, 2020: On the prediction of runup, setup and swash on beaches. *Earth-Sci. Rev.*, **204**, 103148, <https://doi.org/10.1016/j.earscirev.2020.103148>.
- Hedges, T., 1976: An empirical modification to linear wave theory. *Proc. Inst. Civ. Eng.*, **61**, 575–579, <https://doi.org/10.1680/jicp.1976.3408>.
- Holland, K. T., B. Raubenheimer, R. T. Guza, and R. A. Holman, 1995: Runup kinematics on a natural beach. *J. Geophys. Res.*, **100**, 4985–4993, <https://doi.org/10.1029/94JC02664>.
- Holman, R. A., and R. T. Guza, 1984: Measuring run-up on a natural beach. *Coastal Eng.*, **8**, 129–140, [https://doi.org/10.1016/0378-3839\(84\)90008-5](https://doi.org/10.1016/0378-3839(84)90008-5).
- , N. Plant, and T. Holland, 2013: cBathy: A robust algorithm for estimating nearshore bathymetry. *J. Geophys. Res. Oceans*, **118**, 2595–2609, <https://doi.org/10.1002/jgrc.20199>.
- , K. L. Brodie, and N. J. Spore, 2017: Surf zone characterization using a small quadcopter: Technical issues and procedures. *IEEE Trans. Geosci. Remote Sens.*, **55**, 2017–2027, <https://doi.org/10.1109/TGRS.2016.2635120>.
- Honegger, D. A., M. C. Haller, and R. A. Holman, 2019: High-resolution bathymetry estimates via X-band marine radar: 1. Beaches. *Coastal Eng.*, **149**, 39–48, <https://doi.org/10.1016/j.coastaleng.2019.03.003>.
- Huang, Z. C., C. Y. Yeh, K. H. Tseng, and W. Y. Hsu, 2018: A UAV-RTK lidar system for wave and tide measurements in coastal zones. *J. Atmos. Oceanic Technol.*, **35**, 1557–1570, <https://doi.org/10.1175/JTECH-D-17-0199.1>.
- Lin, Y., J. Hyppä, and A. Jaakkola, 2011: Mini-UAV-borne lidar for fine-scale mapping. *IEEE Geosci. Remote Sens. Lett.*, **8**, 426–430, <https://doi.org/10.1109/LGRS.2010.2079913>.
- Ludka, B. C., and Coauthors, 2019: Sixteen years of bathymetry and waves at San Diego beaches. *Sci. Data*, **6**, 161, <https://doi.org/10.1038/s41597-019-0167-6>.
- Martins, K., C. E. Blenkinsopp, and J. Zang, 2016: Monitoring individual wave characteristics in the inner surf with a 2-dimensional laser scanner (lidar). *J. Sens.*, **2016**, 7965431, <https://doi.org/10.1155/2016/7965431>.
- , —, R. Deigaard, and H. E. Power, 2018: Energy dissipation in the inner surf zone: New insights from lidar-based roller geometry measurements. *J. Geophys. Res. Oceans*, **123**, 3386–3407, <https://doi.org/10.1029/2017JC013369>.
- , P. Bonneton, A. Mouragues, and B. Castelle, 2020: Non-hydrostatic, non-linear processes in the surf zone. *J. Geophys. Res. Oceans*, **125**, e2019JC015521, <https://doi.org/10.1029/2019JC015521>.

- O'Dea, A., K. L. Brodie, and P. Hartzell, 2019: Continuous coastal monitoring with an automated terrestrial lidar scanner. *J. Mar. Sci. Eng.*, **7**, 37, <https://doi.org/10.3390/jmse7020037>.
- Power, H. E., M. G. Hughes, T. Aagaard, and T. E. Baldock, 2010: Nearshore wave height variation in unsaturated surf. *J. Geophys. Res.*, **115**, C08030, <https://doi.org/10.1029/2009JC005758>.
- Raubenheimer, B., S. Elgar, and R. T. Guza, 1998: Estimating wave heights from pressure measured in sand bed. *J. Waterw. Port Coastal Ocean Eng.*, **124**, 151–154, [https://doi.org/10.1061/\(ASCE\)0733-950X\(1998\)124:3\(151\)](https://doi.org/10.1061/(ASCE)0733-950X(1998)124:3(151)).
- Sénéchal, N., H. Dupuis, and P. Bonneton, 2004: Preliminary hydrodynamic results of a field experiment on a barred beach, True Vert beach on October 2001. *Ocean Dyn.*, **54**, 408–414, <https://doi.org/10.1007/s10236-003-0052-9>.
- Serafin, K. A., P. Ruggiero, and H. F. Stockdon, 2017: The relative contribution of waves, tides, and non-tidal residuals to extreme total water levels on US West Coast sandy beaches. *Geophys. Res. Lett.*, **44**, 1839–1847, <https://doi.org/10.1002/2016GL071020>.
- Smith, J. M., S. Bak, T. Hesser, M. A. Bryant, and C. Massey, 2017: FRF wave test bed and bathymetry inversion. *Coastal Eng. Proc.*, **1**, 22, <https://doi.org/10.9753/icce.v35.waves.22>.
- Stephens, S. A., G. Coco, and K. R. Bryan, 2011: Numerical simulations of wave setup over barred beach profiles: Implications for predictability. *J. Waterw. Port Coastal Ocean Eng.*, **137**, 175–181, [https://doi.org/10.1061/\(ASCE\)WW.1943-5460.0000076](https://doi.org/10.1061/(ASCE)WW.1943-5460.0000076).
- Stockdon, H. F., R. Holman, P. Howd, and A. H. Sallenger, 2006: Empirical parameterization of setup, swash, and runup. *Coastal Eng.*, **53**, 573–588, <https://doi.org/10.1016/j.coastaleng.2005.12.005>.
- , D. M. Thompson, N. G. Plant, and J. W. Long, 2014: Evaluation of wave runup predictions from numerical and parametric models. *Coastal Eng.*, **92**, 1–11, <https://doi.org/10.1016/j.coastaleng.2014.06.004>.
- Sweet, W. V., and J. Park, 2014: From the extreme to the mean: Acceleration and tipping points of coastal inundation from sea level rise. *Earth's Future*, **2**, 579–600, <https://doi.org/10.1002/2014EF000272>.
- Tebaldi, C., B. H. Strauss, and C. E. Zervas, 2012: Modelling sea level rise impacts on storm surges along US coasts. *Environ. Res. Lett.*, **7**, 014032, <https://doi.org/10.1088/1748-9326/7/1/014032>.
- Thompson, P. R., M. J. Widlansky, M. A. Merrifield, J. M. Becker, and J. J. Marra, 2019: A statistical model for frequency of coastal flooding in Honolulu, Hawaii, during the 21st century. *J. Geophys. Res. Oceans*, **124**, 2787–2802, <https://doi.org/10.1029/2018JC014741>.
- Thornton, E. B., and R. T. Guza, 1982: Energy saturation and phase speeds measured on a natural beach. *J. Geophys. Res.*, **87**, 9499–9508, <https://doi.org/10.1029/JC087iC12p09499>.
- Tissier, M., P. Bonneton, F. Marche, F. Chazel, and D. Lannes, 2012: A new approach to handle wave breaking in fully non-linear Boussinesq models. *Coastal Eng.*, **67**, 54–66, <https://doi.org/10.1016/j.coastaleng.2012.04.004>.
- , —, H. Michallet, and B. G. Ruessink, 2015: Infragravity-wave modulation of short-wave celerity in the surf zone. *J. Geophys. Res. Oceans*, **120**, 6799–6814, <https://doi.org/10.1002/2015JC010708>.
- Turner, I. L., M. D. Harley, and C. D. Drummond, 2016a: UAVs for coastal surveying. *Coastal Eng.*, **114**, 19–24, <https://doi.org/10.1016/j.coastaleng.2016.03.011>.
- , —, A. D. Short, J. A. Simmons, M. A. Bracs, M. S. Phillips, and K. D. Splinter, 2016b: A multi-decade dataset of monthly beach profile surveys and inshore wave forcing at Narrabeen, Australia. *Sci. Data*, **3**, 160024, <https://doi.org/10.1038/sdata.2016.24>.
- Vitousek, S., P. L. Barnard, C. H. Fletcher, N. Frazer, L. Erikson, and C. D. Storlazzi, 2017: Doubling of coastal flooding frequency within decades due to sea-level rise. *Sci. Rep.*, **7**, 1399, <https://doi.org/10.1038/s41598-017-01362-7>.
- Vousdoukas, M. I., T. Kirupakaramoorthy, H. Oumeraci, M. de la Torre, F. Wübbold, B. Wagner, and S. Schimmels, 2014: The role of combined laser scanning and video techniques in monitoring wave-by-wave swash zone processes. *Coastal Eng.*, **83**, 150–165, <https://doi.org/10.1016/j.coastaleng.2013.10.013>.
- , L. Mentaschi, E. Voukouvalas, M. Verlaan, S. Jevrejeva, L. P. Jackson, and L. Feyen, 2018: Global probabilistic projections of extreme sea levels show intensification of coastal flood hazard. *Nat. Commun.*, **9**, 2360, <https://doi.org/10.1038/s41467-018-04692-w>.
- Wallace, L., A. Lucieer, C. Watson, and D. Turner, 2012: Development of a UAV-lidar system with application to forest inventory. *Remote Sens.*, **4**, 1519–1543, <https://doi.org/10.3390/rs4061519>.
- Wojtanowski, J., M. Zygmunt, M. Kaszczuk, Z. Mierczyk, and M. Muzal, 2014: Comparison of 905 nm and 1550 nm semiconductor laser rangefinders' performance deterioration due to adverse environmental conditions. *Opto-Electron. Rev.*, **22**, 183–190, <https://doi.org/10.2478/s11772-014-0190-2>.
- Yamamoto, T., H. L. Koning, H. Sellmeijer, and E. V. Van Hijum, 1978: On the response of a poro-elastic bed to water waves. *J. Fluid Mech.*, **87**, 193–206, <https://doi.org/10.1017/S0022112078003006>.
- Yoo, J., H. M. Fritz, K. A. Haas, P. A. Work, and C. F. Barnes, 2011: Depth inversion in the surf zone with inclusion of wave nonlinearity using video-derived celerity. *J. Waterw. Port Coastal Ocean Eng.*, **137**, 95–106, [https://doi.org/10.1061/\(ASCE\)WW.1943-5460.0000068](https://doi.org/10.1061/(ASCE)WW.1943-5460.0000068).
- Young, A. P., R. T. Guza, H. Matsumoto, M. A. Merrifield, W. C. O'Reilly, and Z. M. Swirad, 2021: Three years of weekly observations of coastal cliff erosion by waves and rainfall. *Geomorphology*, **375**, 107545, <https://doi.org/10.1016/j.geomorph.2020.107545>.